12 Light Scattering

AQ1

Lev T. Perelman

CONTENTS

12.1 INTRODUCTION

Light scattering in biological tissues originates from the tissue inhomogeneities such as cellular organelles, extracellular matrix, blood vessels, etc. This often translates into unique angular, polarization, and spectroscopic features of scattered light emerging from tissue and therefore information about tissue macroscopic and microscopic structure can be obtained from the characteristics of scattered light. Recognition of this fact has led to a long history of the studies of light scattering by biological structures, such as cells and connective tissues.

In 1974, Brunsting et al. performed a series of experiments relating to the internal structure of living cells with the scattering pattern by measuring forward and near-forward scattering in cell suspensions using a rigorous quantitative approach [1]. Later, the researchers used cells of several types such as Chinese hamster's oocytes (CHO), HeLa cells, and nucleated blood cells. They compared the resulting angular distribution of the scattered light with the one predicted by Mie theory, and a very good agreement between the theory and experiment was achieved by approximating a cell as a denser sphere embedded into a larger less-dense sphere. The sizes of these spheres corresponded to the average sizes of the cell nuclei and cells, respectively. The results agree well with scattering theory. Particles that are large compared to a wavelength produce a scattered field that peaks in the forward and near-backward directions in contrast to smaller particles, which scatter light more uniformly. Despite nonhomogeneity and the lack of a perfectly spherical shape of cells and their nuclei, experimental results were well explained using Mie theory, which deals with uniform spheres. These results were supported in the experiments with white blood cells (leukocytes) by Slot et al. [2], who found that light scattering by the leukocytes in the near-forward direction can be explained if each cell was approximated as being composed of two concentric spheres, one being the cell itself and the other being the nucleus, and Hammer et al. [3], who showed that near-forward scattering of light by red blood cells can be accurately described using the van de Hulst approximation, which is derived for large particles of spherical shapes rather than the actual concave–convex disks that are red blood cells.

DK6042_C012.indd 321 10/6/2008 12:48:33 PM

However, most cell organelles and inclusions are themselves complex objects with spatially varying refractive indices [4,5]. Many organelles such as mitochondria, lysosomes, and nuclei possess an average refractive index substantially different from that of their surrounding. Therefore, an accurate model acknowledges subcellular compartments of various sizes with a refractive index different from that of the surrounding.

Mourant et al. found that the cell structures responsible for light scattering can be correlated with the angle of scattering [6]. These studies showed that when a cell is suspended in a buffer solution of lower refractive index, the cell itself is responsible for small angle scattering. This result has been used in flow cytometry to estimate cell sizes [7]. At slightly larger angles, the nucleus is primarily responsible for scattering. It is the major scatterer in forward directions when the cell is a part of a contiguous layer. Smaller organelles, cell inclusions, suborganelles and subnuclear inhomogeneities are responsible for scattering at larger angles. Scattering may originate from organelles themselves or their internal components. Angular dependence may elucidate whether the scattering originates from the objects of regular or irregular shape, spherical or elongated, inhomogeneous or uniform. In some cases, large angle scattering can be attributed to a specific predominant organelle. Research conducted by Beavoit et al. [8] provided strong evidence that mitochondria are primarily responsible for light scattering from hepatocytes.

Components of organelles can also scatter light. Finite-difference time-domain (FDTD) simulations provide means to study spectral and angular features of light scattering by arbitrary particles of complex shape and density. Using FDTD simulations, Drezek et al. [9] investigated the influence of cell morphology on the scattering pattern and demonstrated that as the spatial frequency of refractive index variation increases, the scattering intensity increases at large angles.

Not only does light scattered by cell nuclei have a characteristic angular distribution peaked in the near-backward directions but it also exhibits spectral variations typical for large particles. This information has been used to study the size and shape of small particles such as colloids, water droplets, and cells [10]. The scattering matrix, a fundamental property describing the scattering event, depends not only on the scatterer's size, shape, and relative refractive index but also on the wavelength of the incident light. This method is called light scattering spectroscopy or LSS, and can be very useful in biology and medicine.

Bigio et al. [11] and Mourant et al. [12] demonstrated that spectroscopic features of elastically scattered light can detect transitional carcinoma of the urinary bladder, adenoma and adenocarcinoma of the colon and rectum with good accuracy. In 1998, Perelman et al. observed characteristic LSS spectral behavior in the light backscattered from the nuclei of human intestinal cells [13]. Comparison of the experimentally measured wavelength varying component of light backscattered by the cells with the values calculated using Mie theory, and the size distribution of cell nuclei determined by microscopy demonstrated that both spectra exhibit similar oscillatory behavior. The oscillatory behavior of light scattered by a cell nucleus exhibits frequency dependence with size. This was used to obtain the size distribution of the nuclei from the spectral variation of light backscattered from biological tissues. This method was successfully applied to diagnose precancerous epithelia in several human organs *in vivo* [14–17].

An important aspect of LSS is its ability to detect and characterize particles smaller than the diffraction limit. Particles much larger than the wavelength of light show a prominent backscattering peak and the larger the particle, the sharper the peak [15]. Measurement of 260 nm particles was demonstrated by Backman et al. [18,19] and 100 nm particles by Fang et al. [20]. Scattering from particles with sizes smaller than a wavelength dominates at large angles and does not require an assumption that the particles are spherical or homogenous. Not only is submicron resolution achievable, but it can also be done with larger numerical aperture (NA) confocal optics. By combining LSS with confocal scanning microscopy Itzkan et al. recently identified submicron structures within the cell [21].

12.2 BASIC PRINCIPLES OF LIGHT SCATTERING

Let us consider a particle illuminated by a plane electromagnetic wave

$$\begin{pmatrix} E_{i1} \\ E_{i2} \end{pmatrix} = \begin{pmatrix} E_{01} \\ E_{02} \end{pmatrix} e^{-i(\mathbf{kr}-\omega t)}, \tag{12.1}$$

AQ2

where

E_{i1} and E_{01} are components of the wave amplitude perpendicular to the scattering plane
E_{i2} and E_{02} are components parallel to the scattering plane
k is the wavevector
ω is the frequency

Then the scattering amplitude matrix relates components of the scattered wave (E_{s1}, E_{s2}) and those of the incident one [22]:

$$\begin{pmatrix} E_{s2} \\ E_{s1} \end{pmatrix} = \frac{e^{-i(\mathbf{kr}-\omega t)}}{ikr} \begin{pmatrix} S_2 & S_3 \\ S_4 & S_1 \end{pmatrix} \begin{pmatrix} E_{i2} \\ E_{i1} \end{pmatrix}, \tag{12.2}$$

where $\boldsymbol{r} = \boldsymbol{r}(\theta,\phi)$ is a direction of propagation of the scattered light given by the polar angles θ and ϕ in the spherical system of reference associated with the particle. The scattering amplitude matrix is the fundamental property that gives complete description of the scattering process. For example, the scattering cross section, σ_s, is given by

$$\sigma_s = k^{-2} \int_0^{2\pi} \int_{\pi}^{0} \left(\left| S_1 + S_4 \right|^2 + \left| S_1 + S_4 \right|^2 \right) \mathrm{d}\cos\theta \, \mathrm{d}\phi \tag{12.3}$$

To find the matrix elements of the scattering matrix, one needs to solve Maxwell's wave equations with proper boundary conditions for electric and magnetic fields. Such solution is rather difficult to find; as a matter of fact, there are just a few cases when the analytical solution to the wave equation has been found. In 1907, Gustav Mie obtained the solution for the scattering of a plane wave by a uniform sphere. The functions S_1 and S_2 are expressed as infinite series of Bessel functions of two parameters, *kd* and *kmd*, with *k* the wave number, *d* the diameter of the sphere, and *m* the relative refractive index of the sphere [23]. Other examples of particles for which the scattering problem has been solved analytically are cylinders, coated spheres, uniform and coated spheroids, strips, and planes [19]. Even for these "simple" cases, the amplitudes can be expressed only as infinite series which are often ill converging.

Difficulties with finding exact solutions of the wave equations have led to the development of the approximate methods of solving the scattering problem. One class of those approximations was originally found by Rayleigh in 1871 [22] and is known as Rayleigh scattering. Rayleigh scattering describes light scattering by particles that are small as compared to the wavelength and is a very important approximation for biomedical optics since a great variety of structures cells organelles are built of, such as the tubules of endoplasmic reticulum, cisternae of Golgi apparatus, etc., fall in this category.

In Rayleigh limit, the electric field is considered to be homogenous over the volume of the particle. Therefore, the particle behaves like a dipole and radiates in all directions. In a most relevant case of isotropic polarizability α of the particle, the scattering amplitude matrix becomes

$$\begin{pmatrix} S_2 & S_3 \\ S_4 & S_1 \end{pmatrix} = ik^3\alpha \begin{pmatrix} \cos\theta & 0 \\ 0 & 1 \end{pmatrix}. \tag{12.4}$$

The scattering cross section in this case becomes simply

$$\sigma_s = \frac{8}{3}\pi k^4 \alpha^2. \tag{12.5}$$

Since α is proportional to the particles volume, the scattering cross section scales with particle's linear dimension a as a^6 and varies inversely with λ^4.

For larger particles with sizes comparable to the wavelength, Rayleigh approximation does not work anymore and one can use another solution called Rayleigh–Gans approximation [23]. It is applicable, if the relative refractive index of the particle is close to unity and at the same time the phase shift across the particle $2ka|\Delta m-1|$ is small, where a the linear dimension of the particle and $\Delta m = \frac{\max_{\mathbf{r}\in V}[n(\mathrm{r})]}{\min_{\mathbf{r}\in V}[n(\mathrm{r})]}$. Since the refractive index of most cellular organelles ranges from 1.38 to 1.42 [2,5,8] and the refractive index of the cytoplasm varies from 1.34 to 1.36, both conditions of the Rayleigh–Gans approximation are satisfied for the majority of small organelles.

Rayleigh–Gans approximation is derived by applying the Rayleigh's formulas (Equation 12.4) to any volume element dV within the particle. It can be easily shown that

$$\begin{pmatrix} S_2 & S_3 \\ S_4 & S_1 \end{pmatrix} = \frac{ik^3V}{2\pi}\Re(\theta,\phi)\begin{pmatrix} \cos\theta & 0 \\ 0 & 1 \end{pmatrix}, \tag{12.6}$$

with

$$\Re(\theta,\phi) = \frac{1}{V}\int_V (m(\mathbf{r})-1)\,\mathrm{e}^{i\delta(\mathbf{r},\theta,\phi)}\mathrm{d}\mathbf{r} \tag{12.7}$$

where

$m(\mathbf{r})$ is the relative refractive index at a point $\mathbf{r}$

δ is the phase of the wave scattered in direction (θ,ϕ) by the dipole positioned at a point $\mathbf{r}$

If a particle is relatively homogenous, then

$$\begin{pmatrix} S_2 & S_3 \\ S_4 & S_1 \end{pmatrix} = \frac{ik^3(m-1)V}{2\pi}R(\theta,\phi)\begin{pmatrix} \cos\theta & 0 \\ 0 & 1 \end{pmatrix}, \tag{12.8}$$

where

m is the relative refractive index averaged over the volume of the particle

function $R(\theta,\phi) = \frac{1}{V}\int \mathrm{e}^{i\delta}\mathrm{d}V$ is the so-called form factor

From Equation 12.8 it is easy to see that total intensity of light scattered by a small organelle increases with the increase of its refractive index as $(m-1)^2$ and with its size as a^6. The angular distribution of the scattered light differs from that of Rayleigh scattering. For $\theta = 0$ the form factor equals unity. In other directions, $|R| < 1$, so the scattering has a maximum in forward direction.

Unfortunately, none of the above-mentioned approximations could be applied to the cell nucleus whose size is significantly larger than that of the wavelength. The approximate theory of light scattering by large particles was first proposed by van de Hulst in 1957 [23] and originally formulated for spherical particles only. However, it can be extended to large particles of an arbitrary shape. Although van de Hulst theory does not provide universal rules to find the scattering matrix for all scattering angles even in case of a homogenous sphere, it enables obtaining scattering amplitudes in near-forward direction as well as the scattering cross section.

Let us consider a particle that satisfies the following two conditions: similar to Rayleigh–Gans case the relative refractive index of the particle is close to unity but at the same time opposite to Rayleigh–Gans case, the phase shift across the particle $2ka|\Delta m-1|$ is large. In this case the phase shift will create constructive or destructive interference and we can apply the Huygens' principle and find for the components of the scattering matrix [22]

$$S_{1,2}(\theta) = \frac{k^2}{2\pi}\iint_A (1-\mathbf{e}^{-i\xi(\mathbf{r})})\,\mathrm{e}^{-i\delta(\mathbf{r},\theta)}\mathrm{d}^2\mathbf{r}, \tag{12.9}$$

where

r is a vector in the plane orthogonal to the direction of propagation of the incident light

ξ is the phase shift gained by a light ray that enters the particle at the position given by **r** and passes through the particle along a straight trajectory relative to the phase shift gained by ray propagating outside the particle

δ is the phase difference between the rays scattered by different parts of the particle

The integration is performed over the geometrical cross section of the particle, A. The phase shifts depend on the particle shape and refractive index. For example, for a spherical particle of radius a and relative refractive index m, $\xi = 2ka(m-1)\cos\gamma$ and $\delta = -ka\sin\theta\sin\gamma\cos\varphi$, where γ is an angle between the radial direction and the direction of the initial ray, and φ is an azimuthal angle of a vector oriented toward an element of the surface of the particle. This expression enables one to obtain the scattering amplitude for a large particle of an arbitrary shape.

A well-known expression for the scattering cross section derived by van de Hulst then can be obtained from Equation 12.9 using the optical theorem [22]

$$\sigma_s \approx 2\pi a^2 \left\{1 - \frac{\sin 2x(m-1)}{x(m-1)} + \left[\frac{\sin x(m-1)}{x(m-1)}\right]^2\right\}. \tag{12.10}$$

where $x = ka$ is called the size parameter.

It shows that large spheres give rise to a very different type of scattering than small particles considered above do. Both the intensity of the forward scattering and the scattering cross section are not monotonous functions of wavelength. Rather, they exhibit oscillations with the wavelength; frequency of these oscillations is proportional to $x(m-1)$, so it increases with the sphere size and refractive index.

12.3 LIGHT SCATTERING SPECTROSCOPY

Strong dependence of the scattering cross section (Equation 12.10) on size and refractive index of the scatterer, such as the cell nucleus, as well as on the wavelength seems to suggest that it should be possible to design a spectroscopic technique that could differentiate cellular tissues by the sizes of the nuclei. Indeed, the hollow organs of the body are lined with a thin, highly cellular surface layer of epithelial tissue, which is supported by underlying, relatively acellular connective tissue. There are four main types of epithelial tissues—squamous, cuboidal, columnar, and transitional—which can be found in different organs of the human body. Depending on the type of the epithelium it consists either of a single layer of cells or might have several cellular layers. Here, to make the treatment of the problem more apparent, we will consider epithelial layers consisted of a single well-organized layer of cells, such as simple columnar epithelium or simple squamous epithelium. For example, in healthy columnar epithelial tissues, the epithelial cells often have en-face diameter of 10–20 μm and height of 25 μm. In dysplastic epithelium, the cells proliferate and their nuclei enlarge and appear darker (hyperchromatic) when stained [25].

LSS can be used to measure these changes. The details of the method have been published by Perelman et al. [13] and are only briefly summarized here. Consider a beam of light incident on an epithelial layer of tissue. A portion of this light is backscattered from the epithelial nuclei, while the remainder is transmitted to deeper tissue layers, where it undergoes multiple scattering and becomes randomized before returning to the surface.

Epithelial nuclei can be treated as spheroidal Mie scatters with refractive index, which is higher than that of the surrounding cytoplasm [2,5]. Normal nuclei have a characteristic size of 4–7 μm. In contrast, the size of dysplastic nuclei varies widely and can be as large as 20 μm, occupying almost the entire cell volume. In the visible range, where the wavelength is much smaller than the size of the nuclei, the Van de Hulst approximation (Equation 12.10) can be used

to describe the elastic scattering cross section of the nuclei. Equation 12.10 reveals a component of the scattering cross section that varies periodically with inverse wavelength. This, in turn, gives rise to a periodic component in the tissue reflectance. Since the frequency of this variation (in the inverse wavelength space) is proportional to the particle size, the nuclear size distribution can be obtained from that periodic component.

However, single scattering events cannot be measured directly in biological tissue. Because of multiple scattering, information about tissue scatterers is randomized as light propagates into the tissue, typically over one effective scattering length (0.5–1 mm, depending on the wavelength). Nevertheless, the light in the thin layer at the tissue surface is not completely randomized. In this thin region, the details of the elastic scattering process can be preserved. Therefore, the total signal reflected from tissue can be divided into two parts: single backscattering from the uppermost tissue structures such as cell nuclei, and the background of diffusely scattered light. To analyze the single scattering component of the reflected light, the diffusive background must be removed. This can be achieved either by modeling using DRS [1,26,27] or by other techniques such as polarization background subtraction [28] or coherence gating method [29,30]. AQ3

There are several techniques that can be employed to obtain the nuclear size distribution from the remaining single scattering component of the back-reflected light which can be called the LSS spectrum. A good approximation for the nuclear size distribution can be obtained from the Fourier transform of the periodic component as described in Ref. [1]. A more advanced technique based on linear least squares with a nonnegativity constraints algorithm [31] was introduced by Fang et al. in Ref. 20.

12.4 EARLY CANCER DETECTION WITH LIGHT SCATTERING SPECTROSCOPY

The incidence of adenocarcinoma of the esophagus is increasing more rapidly than any other type of carcinoma in the United States [32]. Almost 100% of cases occur in patients with Barrett's esophagus (BE) [33], a condition in which metaplastic columnar epithelium replaces the normal squamous epithelium of the esophagus. Although the prognosis of patients diagnosed with adenocarcinoma is poor, the chances of successful treatment increase significantly if the disease is detected at the dysplastic stage. The surveillance of patients with BE for dysplasia is challenging in three respects. First, dysplasia is not visible during routine endoscopy [34]. Thus, numerous random biopsy specimens are required. Second, the histopathologic diagnosis of dysplasia is problematic because there is a poor interobserver agreement on the classification of a particular specimen, even among expert gastrointestinal pathologists [35,36]. Third, reliance on histology imposes a time delay between endoscopy and diagnosis, severely limiting the diagnostic accuracy of the endoscopic procedure.

Once BE has been identified, most gastroenterologists will enroll the patient in an endoscopy/biopsy surveillance program, presuming that the patient is a candidate for surgery should high-grade dysplasia (HGD) be detected. Although the cost effectiveness of this type of surveillance program has not been validated in prospective studies, the lack of such studies does not preclude its potential usefulness. Patients with BE who have esophageal carcinoma detected as part of such a surveillance program are more likely to have resectable disease, and have an improved 5 year survival as compared with those whose cancer was detected outside of a surveillance program.

Dysplasia in the gastrointestinal tract is defined as neoplastic epithelium confined within an intact basement membrane. Dysplasia in BE can be classified as low grade or high grade, based on the criteria originally defined for dysplasia in inflammatory bowel disease [37]. Low-grade dysplasia (LGD) is defined primarily by cytological abnormalities, including nuclear enlargement, crowding, stratification, hyperchromasia, mucin depletion, and mitoses in the upper portions of the crypts. These abnormalities extend to the mucosal surface. HGD is characterized by even more pronounced cytological abnormalities, as well as glandular architectural abnormalities including villiform configuration of the surface, branching and lateral budding of the crypts, and formation of the so-called back-to-back glands. When there is any doubt as to the significance of histological abnormalities because of inflammation, ulceration, or histological processing

artifacts, the findings may be classified as indefinite for dysplasia (IND) in order to prevent unnecessary clinical consequences.

Not all patients with BE progress to adenocarcinoma. Some live their entire lives without undergoing malignant or neoplastic transformation. Others demonstrate a rapid progression to carcinoma, and will die of esophageal cancer if it is not diagnosed and treated in a timely manner. Several recent attempts at identifying molecular markers that can predict which patients with BE will progress to esophageal cancer have not been proven effective in clinical trials. For example, anti-p53 antibodies have been shown to develop in patients with BE and adenocarcinoma, and may predate the clinical diagnosis of malignancy [38].

At the present time, the standard of care for surveillance of patients with BE remains debated. Although periodic endoscopic surveillance of patients with BE has been shown to detect carcinoma in its earlier stages, surveillance has significant limitations. Dysplastic and early carcinomatous lesions arising in BE are not visible macroscopically; therefore, surveillance requires extensive random biopsies of the esophagus and histologic examination of the excised tissue for dysplasia. Random biopsy is prone to sampling error (missed dysplastic lesions) and significantly increases the cost and risk of surveillance. There also is a significant interobserver disagreement between pathologists in diagnosing dysplasia. A large, 10 year observational study in 409 patients with BE published in the *British Medical Journal* [39] concluded that the current random biopsy endoscopic surveillance strategy has very limited value. The optical diagnostic technology described in this chapter should be able to address these issues by providing a safe, fast, reliable way to survey the entire length of BE for endoscopically invisible dysplasia.

Similarly, there is no agreement on the most appropriate management of HGD when it is found [40]. Because of the marked variability (range 0%–73%; most often quoted as 33%) in finding unsuspected carcinoma in patients with HGD, esophagectomy is recommended by many clinicians to eliminate the risk of carcinoma or to detect and treat it at an early and treatable stage [41–43]. However, this approach has been criticized because of the high morbidity and mortality associated with esophagectomy, the lack of a systematic biopsy protocol prior to surgery, and the variable natural history of the disease. An important objective of the optical diagnostic technology research is to develop a reliable and sensitive spectroscopic technique to detect and diagnose dysplasia in patients with BE at endoscopy.

The LSS clinical studies described in Ref. [16] were performed on 16 patients with known BE undergoing standard surveillance protocols. The measurements were performed using the LSS system (Figure 12.1). Immediately before biopsy, the reflectance spectrum from that site was collected using an optical fiber probe. The probe was inserted into the accessory channel of the endoscope and brought into gentle contact with the mucosal surface of the esophagus. It delivered a weak pulse of white light to the tissue and collected the reflected light. The probe tip sampled tissue over a circular spot approximately

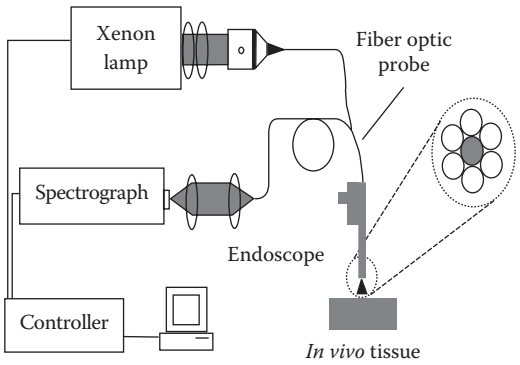

FIGURE 12.1 Schematic diagram of the system used to perform LSS in human subjects undergoing gastroenterological endoscopy procedures. (From Wallace, M., Perelman, L.T., Backman, V., et al., *Gastroentorolgy*, 119, 677, 2000.) AQ4

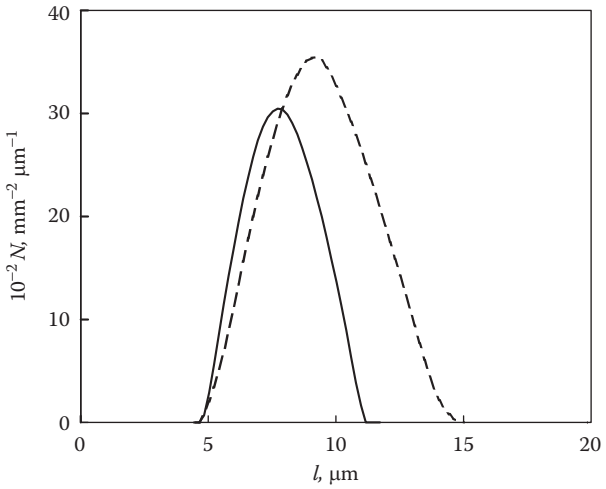

FIGURE 12.2 Nuclear size distributions extracted using LSS technique. Solid line, non-dysplastic site; dashed line, dysplastic site. (From Perelman, L.T., Backman, V., Wallace, M., et al., *Phys. Rev. Lett*., 80, 627, 1998.)

1 mm^2 in area. The pulse duration was 50 ms, and the wavelength range was 350–650 nm. The optical probe caused a slight indentation at the tissue surface that remained for 30–60 s. Using this indentation as a target, the site was then carefully biopsied, and the sample was submitted for histologic examination. This ensured that the site studied spectroscopically matched the site evaluated histologically.

The reflected light was spectrally analyzed, and the spectra were stored in a computer. Example of nuclear size distributions extracted from those spectra for non-dysplastic and dysplastic BE sites are shown in Figure 12.2 [13]. As can be seen, the difference between non-dysplastic and dysplastic sites is pronounced. The distribution of nuclei from the dysplastic site is much broader than that from the non-dysplastic site, and the peak diameter is shifted from ~7 μm to about ~10 μm. In addition, both the relative number of large cell nuclei (>10 μm) and the total number of nuclei are significantly increased. The authors further note that the method provides a quantitative measure of the density of nuclei close to the mucosal surface.

Each site was biopsied immediately after the spectrum was taken. Because of the known large interobserver variation [44], the histology slides were examined independently by four expert GI pathologists. Sites were classified as NDB, IND, LGD, or HGD. On the basis of the average diagnosis [45,46] of the four pathologists, 4 sites were diagnosed as HGD, 8 as LGD, 12 as IND, and 52 as NDB. AQ5 AQ6

To establish diagnostic criteria, eight samples were selected as a "modeling set," and the extracted nuclear size distributions were compared to the corresponding histology findings. From this, the authors decided to classify a site as dysplasia if more than 30% of the nuclei were enlarged, with "enlarged" defined as exceeding a 10 μm threshold diameter, and classified as non-dysplasia otherwise. The remaining 68 samples were analyzed using this criterion. Averaging the diagnoses of the four pathologists [45], the sensitivity and specificity of detecting dysplasia were both 90%, with dysplasia defined as LGD or HGD, and non-dysplasia defined as NDB or IND, an excellent result, given the limitations of interobserver agreement among pathologists.To further study the diagnostic potential of LSS, the entire data set was then evaluated adding a second criterion, the population density of surface nuclei (number per unit area), as a measure of crowding. The resulting binary plot (Figure 12.3) reveals a progressively increasing population of enlarged and crowded nuclei with increasing histological grade of dysplasia, with the NDB samples grouped near the lower left corner and the HGD samples at the upper right. Using logistic regression [47], the samples were then classified by histologic grade as a function of the two diagnostic criteria.

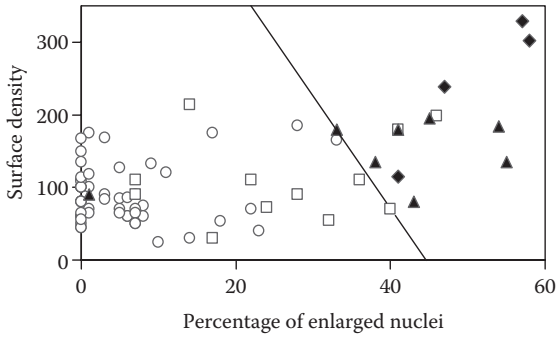

FIGURE 12.3 LSS diagnostic plots of Barrett's esophagus data. NDB–circles; IND–squares; LGD–triangles; HGD–diamonds. The decision threshold for dysplasia is indicated. (From Wallace, M., Perelman, L.T., Backman, V., et al., *Gastroentorolgy*, 119, 677, 2000.)

The percentage agreements between LSS and the average and consensus diagnoses (at least three pathologists in agreement) were 80% and 90%, respectively. This is much higher than that between the individual pathologists and the average diagnoses of their three colleagues, which ranged from 62% to 66%, and this was also reflected in the kappa statistic values [48].

In addition to esophageal epithelium described above, Backman et al. [14] performed a preliminary LSS study for three types of epithelium in three organs: colon (simple columnar epithelium), bladder (transitional epithelium), and oral cavity (squamous stratified epithelium). All studies were performed during routine surveillance procedures. As for the case of BE, all reflectance data were collected *in vivo* with clinical reflectance instruments. Immediately after the measurement, a biopsy sample was taken from the same tissue site and subsequently examined histologically. The results (Figure 12.4) show a clear distinction between normal and diseased epithelium. The dysplastic sites are seen to have a higher percentage of enlarged nuclei and, on average, a higher population density.

These results show the promise of LSS as a real-time, minimally invasive clinical tool for accurately and reliably classifying invisible dysplasia.

12.5 CONFOCAL LIGHT ABSORPTION AND SCATTERING SPECTROSCOPIC MICROSCOPY

Because of its unique optical sectioning properties and due to high sensitivity and specificity of fluorescence molecular probes, confocal fluorescence microscopy established itself as one of the best techniques for studying living cells [49,50]. However, photobleaching and phototoxication of exogenous fluorescence probes make it often difficult to monitor cells for long periods of time. Exogenous fluorescence probes may also modify the cell normal functioning [51]. To address these problems, significant efforts have been recently made to either develop new imaging methods, such as two photon microscopy [52], which are less prone to the above problems, or develop new fluorescent protein probes [53]. At the same time, optical techniques that rely entirely on intrinsic optical properties of tissue for *in vivo* tissue diagnosis such as confocal reflectance microscopy [54], optical coherent tomography [55], LSS [13], and elastic scattering spectroscopy [11] also play a more and more important role.

Recently, a new type of microscopy that also employs intrinsic optical properties of tissue as a source of contrast has been developed [21]. This technique, called confocal light absorption and scattering spectroscopic (CLASS) microscopy, combines LSS recently developed for early cancer detection [4,13–17] with confocal microscopy. In CLASS microscopy, light scattering spectra are the source of the contrast. Another important aspect of LSS is its ability to detect and characterize particles well beyond the diffraction limit. As explained in Perelman and Backman [15], particles much larger than the wavelength of light give rise to a prominent backscattering peak, and the larger

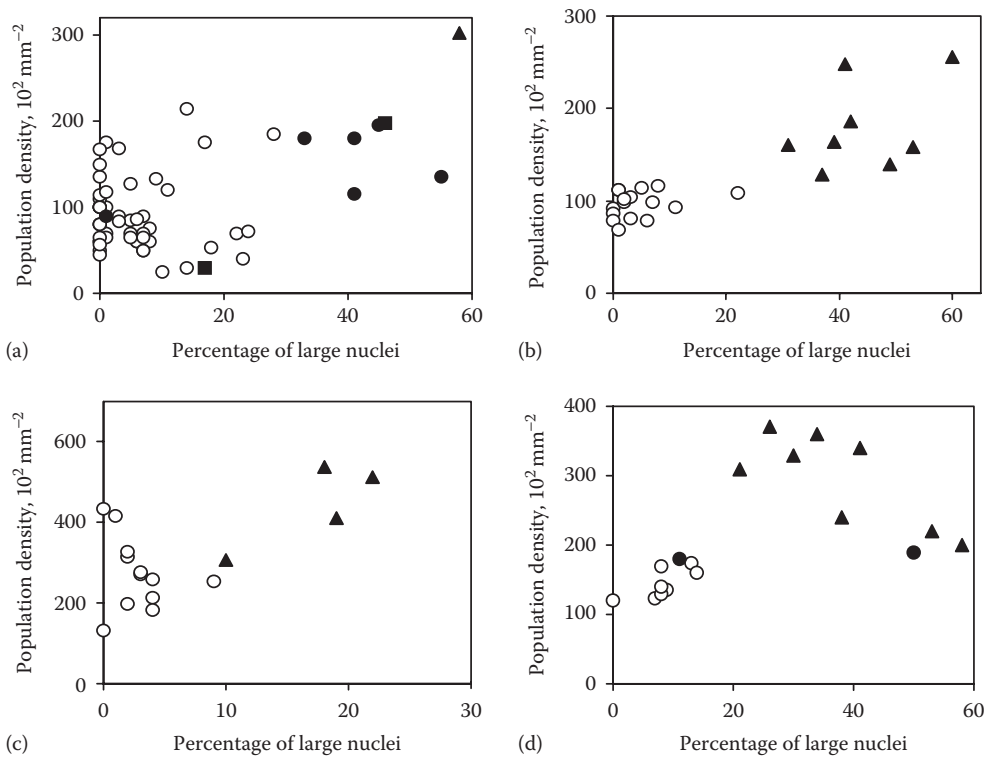

FIGURE 12.4 Dysplasia/CIS classifications for four types of tissues obtained clinically with LSS, compared with histologic diagnosis. In each case, the ordinate indicates the percentage of enlarged nuclei and the abscissa indicates the population density of the nuclei, which parameterizes nuclear crowding. (a) BE: non-dysplastic Barrett's mucosa (circles), indefinite for dysplasia (filled circles), LGD (squares), HGD (triangles); (b) colon: normal colonic mucosa (circles), adenomatous polyp (triangles); (c) urinary bladder: benign bladder mucosa (circles), transitional cell carcinoma *in situ* (triangles); and (d) oral cavity: normal (circles), LGD (filled circles), squamous cell carcinoma *in situ* (triangles). (From Backman, V., Wallace, M., Perelman, L.T., et al., *Nature*, 406, 35, 2000.)

the particle the narrower the angular width of the peak. However, particles with sizes smaller than the wavelength give rise to broad angle backscattering. Thus, the requirement for high NA optics, common in confocal microscopy, is not in conflict with the submicron resolution of LSS. On the contrary, the larger the NA, the larger the contribution of signal from smaller particles.

The CLASS microscope is capable of collecting both spatial and spectroscopic information based on light scattering by submicroscopic biological structures. A schematic of the CLASS microscope is shown in Figure 12.5. Light from the broadband source is delivered through an optical fiber onto a pinhole. The delivery fiber is mounted on a fiber positioner, which allows precise alignment of the fiber relative to the pinhole with the aid of an alignment laser. An iris diaphragm positioned beyond the pinhole is used to limit the beam to match the acceptance angle of the reflective objective. The light beam from the delivery pinhole is partially transmitted through the beam splitter to the sample and partially reflected to the reference fiber. The reflected light is coupled into the reference fiber by the reference collector lens and delivered to the spectrometer. The transmitted light is delivered through an achromatic reflective objective to the sample. Light backscattered from the sample is collected by the same objective and is reflected by the beamsplitter toward the collection pinhole. The collection pinhole blocks most of the light coming from regions

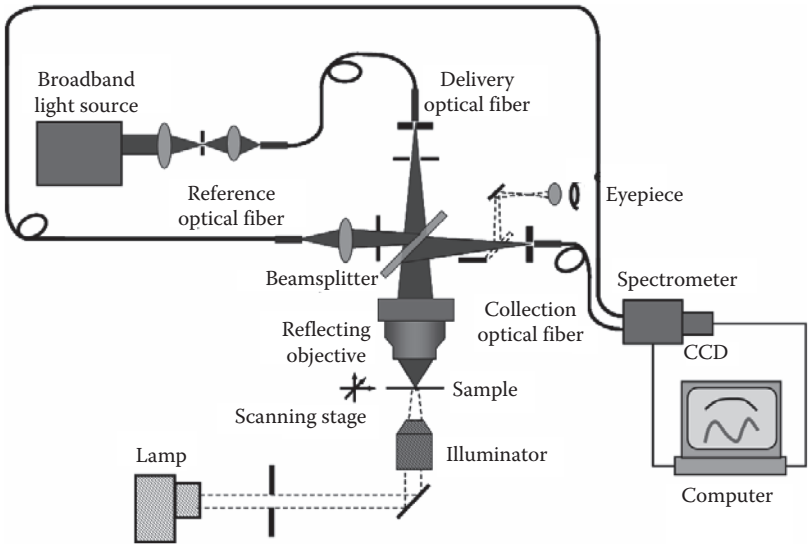

FIGURE 12.5 Schematic of the CLASS microscope. (From Fang, H., Qiu, L., Zaman, M.N., Vitkin, E., Salahuddin, S., Andersson, C., Kimerer, L.M., Cipolloni, P.B., Modell, M.D., Turner, B.S., Keates, S.E., Bigio, I.J., Itzkan, I., Freedman, S.D., Bansil, R., Hanlon, E.B., and Perelman, L.T., *Appl. Opt.* 46, 1760, 2007.)

above and below the focal plane, allowing only the light scattered from a small focal volume to pass through. The light that passes through the pinhole is collected by a second optical fiber for delivery to an imaging spectrograph with a thermo-electrically-cooled CCD detector, which is coupled to a computer. AQ7

Since the experimentally measured CLASS spectrum of a cell is a linear combination of the CLASS spectra of various subcellular organelles with different sizes and refractive indices within the cell, in order to extract these parameters, one can express the experimental spectrum as a sum over organelles' diameters and refractive indices. It is convenient to write this in a matrix form $\hat{S} = \hat{I} \cdot \hat{F} + \hat{E}$, where $\hat{S}$ is the experimental spectrum measured at discrete wavelength points, $\hat{F}$ is a discreet size distribution, $\hat{I}$ is the CLASS spectrum of a single scatterer with diameter d and relative refractive index n, and $\hat{E}$ is the experimental noise [56]. Using the scalar wave model similar to the one developed by Weise et al. [57] and Aguilar et al. [58] it is possible to calculate the CLASS spectrum of a single scatterer $\hat{I}$. In this model, the incident and scattering waves are expanded into the set of plane waves with directions limited by the NA of the objective. The amplitude of the signal detected at the center of the focus through the confocal pinhole is expressed as

$$A(\lambda,\delta,n,\mathrm{NA}) = \int_{-\infty}^{+\infty}\int_{-\infty}^{+\infty} P(-k_X,-k_Y)P(k'_X,k'_Y)\, f\left(\frac{\vec{k}}{k},\frac{\vec{k'}}{k'}\right)\mathrm{d}k_X\mathrm{d}k_Y\mathrm{d}k'_X\mathrm{d}k'_Y, \qquad (12.11)$$

where

λ is the wavelength of both the incident and the scattered light
δ is the diameter of the scatterer
n is the relative refractive index
NA is the numerical aperture of the objective
k' is the wavevector of the incident light
k is the wavevector of the scattered light

P is the objective pupil function
$f\left(\frac{\vec{k}}{k},\frac{\vec{k'}}{k'}\right)$ is the far-field Mie scattering amplitude of the wave scattered in direction $\vec{k}$ created by the incident wave coming from the $\vec{k'}$ direction

To calculate the CLASS spectrum of a single scatterer, one should calculate the scattering intensity, which is just the square of the amplitude, and relate it to the intensity of the incident light, at each wavelength. This gives the following spectral dependence of the CLASS signal:

$$I(\lambda,\delta,n,\mathrm{NA}) = \frac{\left[A(\lambda,\delta,n,\mathrm{NA})\right]^2}{I_0} = \frac{\left[\int_{-\infty}^{+\infty}\int_{-\infty}^{+\infty} P(-k_X,-k_Y)P(k'_X,k'_Y)\, f\left(\frac{\vec{k}}{k},\frac{\vec{k'}}{k'}\right)\mathrm{d}k_X\mathrm{d}k_Y\mathrm{d}k'_X\mathrm{d}k'_Y\right]^2}{\left[\int_{-\infty}^{+\infty}\int_{-\infty}^{+\infty} P(-k_X,-k_Y)P(k'_X,k'_Y)\,\mathrm{d}k_X\mathrm{d}k_Y\mathrm{d}k'_X\mathrm{d}k'_Y\right]^2} \tag{12.12}$$

Since the CLASS spectrum $\hat{I}$ is a highly singular matrix and a certain amount of noise is present in the experimental spectrum $\hat{S}$, it is not feasible to calculate the size distribution $\hat{F}$ by directly inverting the matrix $\hat{I}$. Instead one can multiply both sides of the equation $\hat{S} = \hat{I} \cdot \hat{F} + \hat{E}$ by the transpose matrix $\hat{I}^{\mathrm{T}}$ and introduce the matrix $\hat{C} = \hat{I}^{\mathrm{T}} \cdot \hat{I}$ [56]. Now it should be possible to compute matrix C eigenvalues $\alpha_1,\alpha_2,\ldots$ and sequence them from large to small. This can be done because $\hat{C}$ is a square symmetric matrix. Then, the authors used the linear least squares with nonnegativity constraints algorithm [31] to solve the set of equations

$$\begin{aligned} &\hat{I}^{\mathrm{T}}\hat{S} - (\hat{C} + \alpha_k\hat{H})\hat{F} \to \min \\ &\hat{F} \geq 0 \end{aligned} \tag{12.13}$$

where
$\alpha_k\hat{H}\hat{F}$ is the regularization term
matrix $\hat{H}$ represents the second derivative of the spectrum

The use of the nonnegativity constraint and the regularization procedure is critical to find the correct distribution $\hat{F}$. Thus, by using this algorithm the authors [56] reconstructed the size and refractive index distributions of scattering particles present in the focal volume of the CLASS microscope.

To confirm the ability of CLASS microscope to monitor unstained living cells on submicrometer scale the researchers in Ref. [56] studied human bronchial epithelial cells undergoing apoptosis. Live 16HBE14o- human bronchial epithelial cells were cultured in minimal essential medium (Gibco, Grand Island, New York) with 10% fetal bovine serum, penicillin 100 unit/mL, and streptomycin 100 μg/mL. Cells (50% confluent) were incubated with 100 μM docosahexaenoic acid (DHA) for 24 h to induce apoptosis. Then the cells were detached with trypsin/EDTA, washed in DMEM solution without phenol red and resuspended in the DMEM/OptiPrep solution.

Figure 12.6 presents CLASS reconstructed images of two 16HBE14o- cells. The left cell is a normal untreated cell and the right cell was treated with DHA for 24 h and is undergoing apoptosis. The diameters of the spheres in the image represent the reconstructed sizes of the individual organelles and the gray scale represents their refractive index. Individual organelles can easily be seen inside the cell. In the apoptotic cells, the organelles form shell-like structures with an empty space in the middle. The treated and untreated cells show clear differences in organelle spatial distribution.

The results presented here show that CLASS microscopy is capable of reconstructing images of living cells with submicrometer resolution without use of exogenous markers. Fluorescence microscopy of living cells require application of molecular markers that can affect normal cell

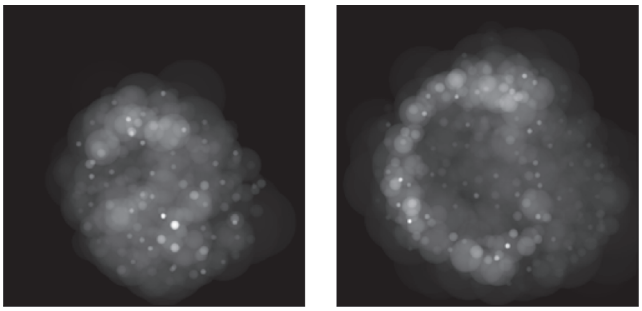

(a) (b)

FIGURE 12.6 Cross-sectional images of two 16HBE14o-human bronchial epithelial cells reconstructed from the CLASS microscope spectra. The left cell (a) is a normal untreated cell and the right cell (b) was treated with DHA for 24 h and is undergoing apoptosis. The diameters of the spheres in the image represent the reconstructed sizes of the individual organelles and the grayscale represents their refractive index. (From Fang, H., Qiu, L., Zaman, M.N., Vitkin, E., Salahuddin, S., Andersson, C., Kimerer, L.M., Cipolloni, P.B., Modell, M.D., Turner, B.S., Keates, S.E., Bigio, I.J., Itzkan, I., Freedman, S.D., Bansil, R., Hanlon, E.B., and Perelman, L.T., *Appl. Opt.* 46, 1760, 2007.)

functioning. In some situations, such as studying embryo development, phototoxication caused by fluorescent tagged molecular markers is not only undesirable but also unacceptable. Another potential problem with fluorescence labeling is related to the fact that multiple fluorescent labels might have overlapping line shapes and this limits number of species that can be imaged simultaneously in a single cell.

CLASS microscopy is not affected by those problems. It requires no exogenous labels and is capable of imaging and continuously monitoring individual viable cells, enabling the observation of cell and organelle functioning at scales on the order of 100 nm. CLASS microscopy can provide not only size information but also information about the biochemical and physical properties of the cell since light scattering spectra are very sensitive to absorption coefficients and the refractive indices, which in turn are directly related to the organelle's biochemical and physical composition (such as the chromatin concentration in nuclei or the hemoglobin concentration and oxygen saturation in red blood cells).

12.6 LIGHT SCATTERING SPECTROSCOPY OF SINGLE NANOPARTICLES

Recently, significant attention has been directed toward the applications of metal nanoparticles to medical problems. Both diagnostic and therapeutic applications have been explored. Metal nanoparticles were also suggested as labels for cancer imaging [59]. Gold nanorods have the potential to be employed as extremely bright molecular marker labels for fluorescence, absorption, or scattering imaging of living tissue. However, samples containing a large number of gold nanorods usually exhibit relatively wide spectral lines. This linewidth would limit the use of the nanorods as effective molecular labels, since it would be rather difficult to image several types of nanorod markers simultaneously. In addition, the observed linewidth does not agree well with theoretical calculations, which predict significantly narrower absorption and scattering lines.

As shown in Ref. [60], the discrepancy is explained by the apparent line broadening because of the contribution of nanorods with various sizes and aspect ratios. That suggests that nanorod-based molecular markers with a narrow aspect ratio and, to a lesser degree size distributions, should provide spectral lines sufficiently narrow for effective biomedical imaging.

Nanoparticles with sizes small compared to the wavelength of light made from metals with a specific complex index of refraction, such as gold and silver, have absorption and scattering

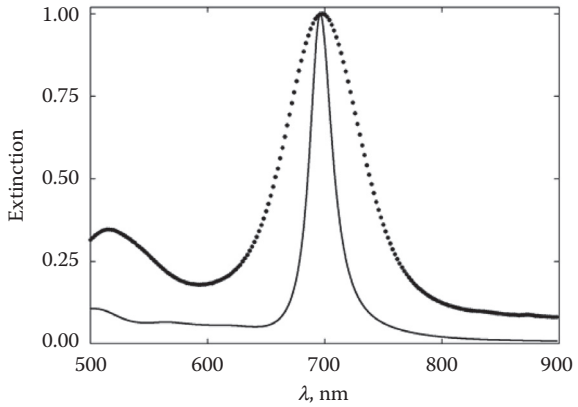

FIGURE 12.7 Optical properties of an ensemble of gold nanorods. Normalized extinction of the same sample of gold nanorods in aqueous solution as in the TEM image. Dots—experiment; dashed line—T-matrix calculation for a single-size nanorod with length and width of 48.9 nm and 16.4 nm, respectively. (From Qiu, L., Larson, T.A., Smith, D.K., Vitkin, E., Zhang, S., Modell, M.D., Itzkan, I., Hanlon, E.B., Korgel, B.A., Sokolov, K.V., and Perelman, L.T., *IEEE J. Selected Top. Quantum Electron*., 13, 1730, 2007.) AQ8

resonance lines in the visible part of the spectrum. These lines are due to in-phase oscillation of free electrons and are called surface plasmon resonances.

In Ref. [60], the researchers performed optical transmission measurements of gold nanorod spectra in aqueous solutions using a standard transmission arrangement for extinction measurements described in Ref. [61]. Concentrations of the solutions were chosen to be close to 10^{10} nanoparticles per milliliter of the solvent to eliminate optical interference. The measured longitudinal plasmon mode of the nanorods is presented as a dotted curve on Figure 12.7. It shows that multiple nanorods in aqueous solution having width at half maximum of approximately 90 nm. This line is significantly wider than the line one would get from either T-matrix calculations or dipole approximation. Solid line on Figure 12.7 shows plasmon spectral line calculated with the T-matrix calculations for nanorods with the length and width of 48.9 nm and 16.4 nm, respectively. The theoretical line is also centered at 700 nm but has a width of approximately 30 nm.

The CLASS system with the supercontinuum broadband laser source described in Ref. [21] is at present uniquely capable of performing single nanoparticle measurements. It is capable of collecting both spatial (imaging) and spectroscopic information based on light scattering by submicroscopic structures. To illustrate that individual gold nanorods indeed exhibit narrow spectral lines, the authors in Ref. [60] detected single gold nanorods with the CLASS system and measured their scattering spectra.

To measure scattering from individual gold nanorods, diluted aqueous samples of gold nanorods were scanned with the CLASS system and images were acquired, which show locations of the individual gold nanorods. The system measured scattering spectra of several single gold nanorods. One can see (Figure 12.8) that typical single gold nanorod exhibit spectrum that is significantly narrower than the spectrum collected from the nanorods distribution. By comparing these measurements with the numerical calculations based on the T-matrix approach that utilized the complex refractive index of gold from Ref. [62], the researchers found an excellent agreement with the theory [60].

Using the CLASS instrument, the researchers have detected plasmon scattering spectra of single gold nanorods. From these measurements, one can draw the conclusion that single gold nanorods exhibit a scattering line significantly narrower than the lines routinely observed in experiments that involve multiple nanorods. Narrow, easily tunable spectra would allow several biochemical species to be imaged simultaneously with molecular markers which employ gold nanorods of several different

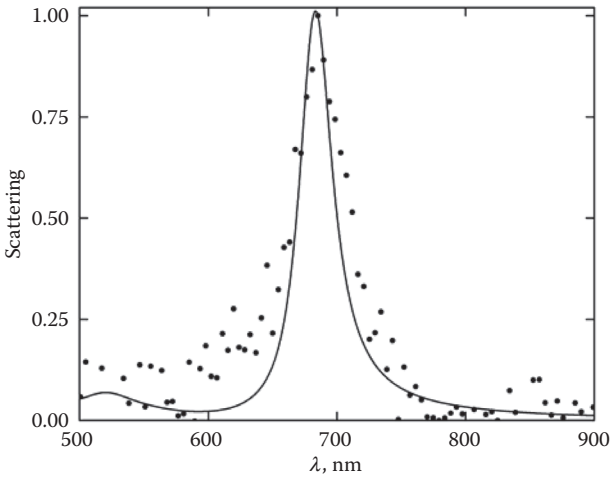

FIGURE 12.8 Normalized scattering spectrum for single gold nanorod. Dots—CLASS measurements, solid lines—T-matrix calculation for nanorods with 3.3 aspect ratio and 16.2 nm width. (From Qiu, L., Larson, T.A., Smith, D.K., Vitkin, E., Zhang, S., Modell, M.D., Itzkan, I., Hanlon, E.B., Korgel, B.A., Sokolov, K.V., and Perelman, L.T., *IEEE J. Selected Top. Quantum Electron*., 13, 1730, 2007.)

aspect ratios as a label. These markers could be used for cellular microscopic imaging where even a single nanorod could be detected. Minimizing the number of nanoparticles should reduce possible damage to a living cell. For optical imaging of tumors, multiple gold nanorods with a narrow aspect ratio distribution might be used. A possible technique for obtaining a narrow aspect ratio distribution might employ devices already developed for cell sorting. These would use the position of the narrow plasmon spectral line for particle discrimination.

12.7 CONCLUSIONS

Emerging light-scattering-based techniques such as LSS and CLASS discussed in this chapter are capable of providing quantitative morphological diagnostic information about tissues and cells *in vivo*. This is a unique capability since methods for providing such information without tissue removal are not currently available. They are nondestructive and do not require the contrast agents common to many other optical techniques since they employ light scattering spectra as a source of the native contrast. Since they rely on multiwavelength spectral information to extract sizes of the scatteres, they are not diffraction limited. Applications for light-scattering-based techniques in such diverse areas as clinical medicine, cell biology, and drug discovery are all linked by the potential of these techniques to observe functional intracellular processes nondestructively.

ACKNOWLEDGMENT

This work was supported by NIH Grants No. R01EB003472 and No. RR017361.

REFERENCES

1. Brunsting A and Mullaney F. Differential light scattering from spherical mammalian cells, *Biophys. J.*, 14, 439–453, 1974.
2. Sloot PMA, Hoekstra AG, and Figdor CG. Osmotic response of lymphocytes measured by means of forward light-scattering—theoretical considerations, *Cytometry*, 9, 636–641, 1988.
3. Hammer M, Schweitzer D, and Michel B. Single scattering by red blood cells, *Appl. Opt*., 37, 7410–7418, 1998.

4. Backman V, Gurjar R, Badizadegan K, Dasari RR, Itzkan I, and Perelman LT, Feld MS. Polarized light scattering spectroscopy for quantitative measurement of epithelial cellular structures *in situ*, *IEEE J. Selected Top. Quantum Electron*., 5, 1019–1027, 1999.
5. Beuthan J, Milnet O, and Helfmann J. The spatial variation of the refractive index in biological cells, *Phys. Med. Biol*., 41, 369–382, 1996.
6. Mourant JR, Freyer JP, Hielscher AH, Eick AA, Shen D, and Johnson TM. Mechanisms of light scattering from biological cells relevant to noninvasive optical-tissue diagnosis, *Appl. Opt*., 37, 3586–3593, 1998.
7. Watson JV, *Introduction to Flow Cytometry*, Cambridge University Press, Cambridge, 1991.
8. Beauvoit B, Kitai T, and Chance B. Contribution of the mitochondrial compartment to the optical properties of rat liver: A theoretical and practical approach, *Biophys. J*., 67, 2501–2510, 1994.
9. Drezek R, Dunn A, and Richards-Kortum R. Light scattering from cells: finite-difference time-domain simulations and goniometric measurements, *Appl. Opt*., 38, 3651–3661, 1999.
10. Newton RG, *Scattering Theory of Waves and Particles*, McGraw-Hill Book Company, New York, 1969.
11. Bigio IJ and Mourant JR. Ultraviolet and visible spectroscopies for tissue diagnostics: Fluorescence spectroscopy and elastic-scattering spectroscopy, *Phys. Med. Biol.,* 42, 803–814, 1997.
12. Mourant JR, Boyer J, Johnson T, et al. Detection of gastrointestinal cancer by elastic scattering and absorption spectroscopies with the Los Alamos Optical Biopsy System, *Proc. SPIE*, 2387, 210–217, 1995.
13. Perelman LT, Backman V, Wallace M, et al. Observation of periodic fine structure in reflectance from biological tissue: A new technique for measuring nuclear size distribution, *Phys. Rev. Lett*., 80, 627–630, 1998.
14. Backman V, Wallace M, Perelman LT, et al. Detection of preinvasive cancer cells. Early-warning changes in precancerous epithelial cells can now be spotted *in situ*, *Nature*, 406(6791), 35–36, 2000.
15. Perelman LT and Backman V. Chapter XII. Light scattering spectroscopy of epithelial tissues: Principles and applications. In: Tuchin V, editor, *Handbook on Optical Biomedical Diagnostics*, SPIE Press, Bellingham, pp. 675–724, 2002.
16. Wallace M, Perelman LT, Backman V, et al. Endoscopic detection of dysplasia in patients with Barrrett's esophagus using light scattering spectroscopy, *Gastroentorolgy*, 119, 677–682, 2000.
17. Gurjar R, Backman V, Perelman LT, et al. Imaging human epithelial properties with polarized light scattering spectroscopy, *Nat. Med*., 7, 1245–1248, 2001.
18. Backman V, Gopal V, Kalashnikov M, et al. Measuring cellular structure at submicrometer scale with light scattering spectroscopy, *IEEE J. Selected Top. Quantum Electron*., 7, 887–893, 2001.
19. Backman V, Gurjar R, Perelman LT, et al. Imaging and measurement of cell organization with submicron accuracy using light scattering spectroscopy. In: Alfano RR, editor, *Optical Biopsy IV*, Proceedings of SPIE, 4613, pp. 101–110, 2002. AQ9
20. Fang H, Ollero M, Vitkin E, et al. Noninvasive sizing of subcellular organelles with light scattering spectroscopy, *IEEE J. Selected Top. Quantum Electron*., 9, 267–276, 2003.
21. Itzkan I, Qui L, Fang H, et al. Confocal light absorption & scattering spectroscopic (CLASS) microscopy monitors organelles in live cells with no exogenous labels, *Proc. Natl. Acad. Sci. U. S. A*., **104**, 17255–17260, 2007.
22. Newton RG. *Scattering Theory of Waves and Particles*, McGraw-Hill Book Company, New York, 1969.
23. van de Hulst HC. *Light Scattering by Small Particles*, Dover Publications, New York, 1957.
24. Kerker M. *The Scattering of Light*, Academic Press, New York, 1969. AQ10
25. Cotran RS, Robbins SL, and Kumar V. *Pathological Basis of Disease*, W. B. Saunders Company, Philadelphia, 1994.
26. Zonios G, Perelman LT, Backman V, et al. Diffuse reflectance spectroscopy of human adenomatous colon polyps in vivo, *Appl. Opt*., 38, 6628–6637, 1999.
27. Georgakoudi I, Jacobson BC, Van Dam J, et al. Fluorescence, reflectance and light scattering spectroscopies for evaluating dysplasia in patients with Barrett's esophagus, *Gastroentorolgy*, 120, 1620–1629, 2001.
28. Backman V, Gurjar R, Badizadegan K, et al. Polarized light scattering spectroscopy for quantitative measurement of epithelial cellular structures in situ, *IEEE J. Selected Top. Quantum Electron*., 5, 1019–1027, 1999.
29. Pyhtila JW, Graf RN, and Wax A. Determining nuclear morphology using an improved angle-resolved low coherence interferometry system, *Opt. Express*, 11, 3473–3484, 2003.
30. Graf R and Wax A. Nuclear morphology measurements using Fourier domain low coherence interferometry, *Opt. Express*, 13, 4693–4698, 2005.
31. Craig IJD and Brown JC, *Inverse Problems in Astronomy: A Guide to Inversion Strategies for Remotely Sensed Data*, A. Hilger, 1986. AQ11

32. Blot W, Devesa SS, Kneller R, and Fraumeni J. Rising incidence of adenocarcinoma of the esophagus and gastric cardia, *J Am. Med. Assoc*., 265, 1287–1289, 1991.
33. Antonioli D. The esophagus. In: Henson D and Alobores-Saavdera J, editors, *The Pathology of Incipient Neoplasia*, Saunders, Philadelphia, pp. 64–83, 1993.
34. Cameron AJ. Management of Barrett's esophagus, *Mayo Clin. Proc*., 73, 457–461, 1998.
35. Reid BJ, Haggitt RC, Rubin CE, et al. Observer variation in the diagnosis of dysplasia in Barrett's esophagus, *Hum. Pathol*., 19, 166–178, 1988.
36. Petras RE, Sivak MV, and Rice TW. Barrett's esophagus. A review of the pathologist's role in diagnosis and management, *Pathol. Annual*., 26, 1–32, 1991.
37. Riddell RH, Goldman H, Ransohoff DF, et al. Dysplasia in inflammatory bowel disease: Standardized classification with provisional clinical applications, *Hum. Pathol*., 14, 931–86, 1983.
38. Cawley HM, Meltzer SJ, De Benedetti VM, et al. Anti-p53 antibodies in patients with Barrett's esophagus or esophageal carcinoma can predate cancer diagnosis, *Gastroenterology*, 115, 19–27, 1998.
39. Macdonald CE, Wicks AC, and Playford RJ. Final results from 10 year cohort of patients undergoing surveillance for Barrett's oesophagus: Observational study, *Br. Med. J.,* 321, 1252–1255, 2000.
40. Falk GW, Rice TW, Goldblum JR, et al. Jumbo biopsy forceps protocol still misses unsuspected cancer in Barrett's esophagus with high-grade dysplasia, *Gastrointest. Endosc*., 49, 170–176, 1999.
41. Altorki NK, Sunagawa M, Little AG, et al. High-grade dysplasia in the columnar-lined esophagus, *Am. J. Surg*., 161, 97–100, 1991.
42. Pera M, Trastek VF, Carpenter HA, et al. Barrett's esophagus with high-grade dysplasia: An indication for esophagectomy, *Ann. Thorac. Surg*., 54, 199–204, 1992.
43. Rice TW, Falk GW, Achkar E, et al. Surgical management of high-grade dysplasia in Barrett's esophagus, *Am. J. Gastroenterol*., 88, 1832–1836, 1993.
44. Reid BJ, Haggitt RC, Rubin CE, et al. Observer variation in the diagnosis of dysplasia in Barrett's esophagus, *Hum. Pathol*., 19, 166–178, 1988.
45. Riddell RH, Goldman H, Ransohoff DF, et al., Dysplasia in inflammatory bowel disease: Standardized classification with provisional clinical applications, *Hum. Pathol*., 14, 931–986, 1983.
46. Haggitt RC. Barrett's esophagus, dysplasia, and adenocarcinoma, *Hum. Pathol*., 25, 982–993, 1994.
47. Pagano M and Gauvreau K. *Principles of Biostatistics*, Duxbury Press, Belmon, CA, 1993.
48. Landis J, and Koch G. The measurement of observer agreement for categorical data, *Biometrics*, 33, 159–174, 1977.
49. Conchello J-A and Lichtman JW. Optical sectioning microscopy, *Nat. Methods*, **2**, 920–931, 2005.
50. Lippincott-Schwartz J and Patterson GH. Development and use of fluorescent protein markers in living cells, *Science*, 300, 87–91, 2003.
51. Lichtman JW and Confchello J-A. Fluorescence microscopy, *Nat. Methods*, 2, 910–919, 2005.
52. Zipfel WR, Williams RM, and Webb WW. Nonlinear magic: Multiphoton microscopy in the biosciences, *Nat. Biotechnol*., 21, 1369–1377, 2003.
53. Shaner NC, Steinbach PA, and Tsien RY. A guide to choosing fluorescent proteins, *Nat. Methods*, 2, 905–909, 2005.
54. Dwyer PJ, Dimarzio CA, Zavislan JM, et al. Confocal reflectance theta line scanning microscope for imaging human skin in vivo, *Opt. Lett*., 31, 942–944, 2006.
55. Fujimoto JG. Optical coherence tomography for ultrahigh resolution in vivo imaging, *Nat. Biotechnol*., 21, 1361–1367, 2003.
56. Fang H, Qiu L, Zaman MN, et al. Confocal light absorption and scattering spectroscopic (CLASS) microscopy, *Appl. Opt*., 46, 1760–1769, 2007.
57. Weise W, Zinin P, Wilson T, et al. Imaging of spheres with the confocal scanning optical microscope, *Opt. Lett*., 21, 1800–1802, 1996.
58. Aguilar JF, Lera M, and Sheppard CJR. Imaging of spheres and surface profiling by confocal microscopy, *Appl. Opt*., 39, 4621–4628, 2000.
59. Durr NJ, Larson T, Smith DK, et al. Two-photon luminescence imaging of cancer cells using molecularly targeted gold nanorods, *Nano Lett*., 7, 941–945, 2007.
60. Qiu L, Larson TA, Smith DK, et al. Single gold nanorod detection using confocal light absorption and scattering spectroscopy, *IEEE J. Selected Top. Quantum Electron*., 13, 1730–1738, 2007.
61. Bohren CF and Huffman DR, *Absorption and Scattering of Light by Small Particels*, John Wiley & Sons, New York, 1983.
62. Johnson PB and Christy RW, Optical constants of noble metals, *Phys. Rev. B*, 6, 4370–4379, 1972.